ScieRxiv
NOT PEER-REVIEWED
Article

Polydopamine-derived Co_3O_4/N-carbon heterostructures anchored with gold nanorods for high-performance plasmonic-assisted zinc-air batteries

Valentín García-Caballero[1], Domingo Salazar-Ordoñez[1], Juan J. Giner-Casares[1], Mónica Calero[2], Mario J. Muñoz-Batista[2], Manuel Cano[1,*], Antonio J. Fernández Romero[1,*]

[1]Departamento de Química Física y Termodinámica Aplicada, Instituto Químico para la Energía y el Medioambiente (IQUEMA), Universidad de Córdoba, E-14014 Córdoba, Spain.
[2]Department of Chemical Engineering, University of Granada, 18071 Granada, Spain.

[*]**Correspondence to:** Dr. Manuel Cano, Prof. Antonio J. Fernández-Romero, Departamento de Química Física y Termodinámica Aplicada, Instituto Químico para la Energía y el Medioambiente (IQUEMA), Universidad de Córdoba (UCO), E-14014 Córdoba, Spain. E-mail: q82calum@uco.es; qf2feroa@uco.es

Received: 03 November 2026 | Approved: 16 November 2026 | Online: 16 November 2026

Abstract

Rechargeable zinc–air batteries (ZABs) offer an exceptionally high theoretical energy density by utilizing atmospheric oxygen as a reactant, rendering them a safer, significantly more compact and lightweight than conventional energy storage devices. However, their practical round-trip efficiency is severely hindered during recharging by the sluggish kinetics and high overpotentials associated with the oxygen evolution reaction (OER). To address this bottleneck, this study investigates the plasmonic-enhancement effect on the ZAB system by anchoring gold nanorods (AuNRs) onto an advanced air electrode composed of Co_3O_4/nitrogen-doped carbon (Co_3O_4/N-Carbon)

© The Author(s) 2026. Open Access This article is licensed under a Creative Commons Attribution 4.0 International License (https://creativecommons.org/licenses/by/4.0/), which permits unrestricted use, sharing, adaptation, distribution and reproduction in any medium or format, for any purpose, even commercially, as long as you give appropriate credit to the original author(s) and the source, provide a link to the Creative Commons license, and indicate if changes were made.

heterostructures. This carbon matrix was synthesized utilizing polydopamine (PDA) as a precursor to ensure the robust retention of structural nitrogen networks. Comprehensive structural and morphological characterization confirmed the uniform distribution and synergistic integration of Co_3O_4 phase and AuNRs over the N-Carbon architecture. Electrochemical analysis revealed that near-infrared (NIR) laser illumination substantially accelerates the electrocatalytic OER kinetics. However, adjusting the AuNR loading is fundamental, as excessive concentration causes a detrimental shielding effect that inhibits the active catalytic sites. Furthermore, the incorporation of AuNRs facilitates a dark electron transfer across the heterojunction from Co_3O_4 to Au, leaving the latter with an excess of negative charge. This modification of charge transport dynamics, combined with the plasmonic effect of AuNRs under NIR irradiation, significantly enhances performance. When integrated into a working ZAB under *in situ* laser NIR radiation, significantly enhances the charging process, although an improvement in the discharge process is also observed, even at current densities as high as 31.8 mA cm^{-2}. At 0.16 mA cm^{-2}, a round-trip efficiency of 82.4 % has been achieved. These findings provide a novel and strategic paradigm for designing high-performance, light-assisted electrochemical energy storage and conversion systems.

Keywords: Zinc–air batteries, localized surface plasmon resonance (LSPR), gold nanorods, cobalt oxide, polydopamine-derived carbon, photo-assisted electrocatalysis, plasmonic batteries

INTRODUCTION

Electrochemical energy conversion and storage systems (EECS) play a key role in the global energy transition, as global energy demand shifts from fossil fuels to renewable sources. Among various EECS devices, metal-air batteries and, in particular, zinc-air batteries (ZABs) have attracted significant attention due to their high theoretical energy density, low cost, and environmental friendliness[1,2]. Although ZABs are the only commercial metal-air batteries, they are non-rechargeable primarily due to the sluggish oxygen evolution reaction (OER), which constitutes a major bottleneck. The OER is a complex four-electron process that inherently suffers from a high thermodynamic overpotential. Currently, precious metal, as Pt, or Pd, and metal oxides like IrO_2 and RuO_2 serve as the benchmark OER catalysts. However, their widespread industrial

application remains severely limited by high costs and the scarcity of noble metal precursors. Consequently, developing efficient earth-abundant, and low-cost OER electrocatalysts is a paramount challenge in renewable energy research. Transition-metal-based materials—specifically oxides, hydroxides, and oxyhydroxides of Fe, Co, Ni, or Mn—have emerged as highly promising alternatives. These materials are economically viable, exhibit remarkable electrocatalytic activity in alkaline media, and demonstrate excellent long-term operational stability[3,4].

The most significant recent developments in this direction have focused on Co_3O_4-based catalysts. Co_3O_4 has emerged as a promising candidate for OER because of several factors: 1) the spinel structure of Co_3O_4 features Co^{2+} ions occupying tetrahedral sites and Co^{3+} ions residing in octahedral sites within a cubic close-packed oxygen lattice. This unique arrangement facilitates electron transfer between the different cobalt valence states, which is crucial for multi-step electrochemical reactions like OER; 2) Co_3O_4 exhibits high chemical stability under harsh alkaline conditions, thereby enabling the development of ultra-stable electrocatalysts for alkaline ZABs[5].

On the other hand, although the coexistence of mixed-valence states enables performance in both oxidation and reduction reactions, Co_3O_4 inherently exhibits poor ORR catalytic activity. To mitigate this limitation, enhance its ORR performance, and consequently boost its bifunctional capability, the *in situ* growth of this oxide on various heteroatom-doped (e.g., N or P) carbonaceous materials has recently emerged as a highly effective strategy[6].

In this regard, S. Liu *et al.* investigated the synergistic activity of Co_3O_4 grown onto an N-doped carbon nanoweb (CNW) as a bifunctional electrocatalyst for both the ORR and OER. The authors suggested that within the composite material, the CNW serves as the primary catalyst for the ORR, whereas Co_3O_4 facilitates a four-electron ORR pathway over the two-electron process. Conversely, during the OER, Co_3O_4 acts as the primary catalytic site while simultaneously preventing CNW degradation, while CNW enhances electron transfer to the current collector[7].

Recently, photoactive materials capable of harvesting light across the UV-visible-NIR spectrum have been proposed for positive electrodes to accelerate the kinetics of the ORR

and OER in alkaline media, thereby enhancing the overall efficiency of ZABs. These materials convert solar energy into electrochemical energy to boost the discharge voltage or lower the overpotential required during charging, thus minimizing the energy input needed for recharging. While the majority of currently developed materials exhibit photoactivity exclusively toward either the ORR or the OER, bifunctional catalysts active in both processes are essential to maximize round-trip efficiency in ZABs. Consequently, various photoactive electrodes incorporating advanced semiconductor materials have been engineered to optimize ORR and OER electrocatalysis in next-generation ZABs[8-12].

In 2020, Zhu *et al.*[11] designed a three-electrode zinc-air battery (ZAB) featuring a metallic Zn plate as the negative electrode and two distinct positive photoelectrodes. One photoelectrode was dedicated to the discharge process (based on poly(1,4-di(2-thienyl))benzene), while the other was utilized for recharging (a TiO_2-based photocathode). In this configuration, the battery delivers a significantly higher potential during discharge than the voltage required for recharging, yielding a round-trip efficiency above 100%. Subsequently, Feng *et al.*[12] integrated a TiO_2/In_2Se_3 heterojunction as a bifunctional photocathode to develop a two-electrode ZAB. When discharged at a current density of 0.1 mA cm^{-2}, this system achieved a discharge voltage of 1.79 V *vs.* SHE, which is 149 mV higher than the theoretical value for conventional ZABs. Furthermore, the charging voltage reached only 0.67 V, sitting well below the theoretical threshold. Consequently, the discharging potential exceeded the charging potential by 1.12 V, demonstrating that the battery generates substantially more energy during discharge than it consumes during charging. This phenomenon is driven by the simultaneous conversion of light energy into electrochemical energy during both processes. Notably, even at a higher current density of 10 mA cm^{-2}, the discharge potential (1.23 V *vs.* SHE) remained superior to the charging voltage (1.16 V *vs.* SHE).

However, semiconductor-based photocathodes typically have low absorption coefficients, large bandgap energies (mostly in the UV-Visible region), short charge carrier diffusion lengths and lifetimes, and consequently, slow reaction kinetics at their surface[13]. Furthermore, in recent years a great effort has been made to improve the optical, electrical and catalytic properties of photocathodes. Among others, one promising solution is to combine plasmonic nanoparticles (PNPs) and semiconducting

photocatalytic materials[14-16]. To exhibit plasmonic behavior, these PNPs are primarily composed of materials with a high density of free conduction electrons, most commonly noble metals such as gold (Au), silver (Ag), or copper (Cu).

Under appropriate incident electromagnetic radiation, PNPs exhibit a coherent oscillation of conduction electrons, known as localized surface plasmon resonance (LSPR). Thus, PNPs generate intense local electromagnetic fields and transfer energy to the united semiconductor by four different mechanisms[14]. This energy transfer causes an increase of semiconductor absorption, by either confining or scattering the light into the semiconductor. Additionally, PNPs can extend the semiconductor absorption range, because they absorb light with higher wavelengths (lower energies) than the semiconductor bandgap and subsequently transfer the absorbed energy to the semiconductor as “hot electrons” or by a dipole-dipole interaction. Thus, this synergetic dual-field increases photocurrent in several orders, due to efficient charge accumulation and separation, inhibiting recombination, and enable directional electron transport, improving the electronic and catalytic properties of the semiconductors. In this sense, several chemical reactions, such as ORR, OER and HER have been mediated by PNPs alone or forming semiconductors junctions[14-17].

To date, few studies have been published that employ plasmonic materials to enhance battery performance; all of these involve Li-based batteries, which typically use non-aqueous electrolytes[18-21]. For instance, Zheng *et al.* successfully immobilized silver nanoparticles on carbon cloth (Ag@CC), demonstrating that localized surface plasmon resonance (LSPR) thermal and hot-electron effects could simultaneously accelerate both ORR and OER kinetics as a high-performance bifunctional catalyst in aprotic Li-O_2 batteries[20].

Recently, Ma *et al.* engineered an Au–TiO_2 heterojunction deployed as a high-performance photocathode in photo-assisted lithium-ion batteries[21]. This architecture was synthesized by embedding the plasmonic metal entities within the TiO_2 matrix, thereby establishing localized Schottky barriers at the metal–semiconductor interfaces. Under specific illumination, this energy barrier is effectively lowered, synergistically assisted by the intrinsic electronic conductivity, the generation of oxygen vacancies, and the light-harvesting capability of the host TiO_2. This configuration consequently

expedites efficient hot-electron injection from the metal domain into the semiconductor conduction band. Similarly, Li *et al.* investigated the photo-irradiation effect on a composite catalyst consisting of gold nanoparticles (AuNPs) anchored onto Co–FeOOH[22]. They demonstrated that visible-light illumination substantially augmented the electrocatalytic efficiency toward the OER, concluding that the plasmon-induced excitation of hot electrons significantly promotes the generation of highly active catalytic sites and reactive species at the surface.

Furthermore, Zhen and co-workers investigated three distinct interfaces between plasmonic Au nanostructures (nanoflowers, films, and nanoshells) and a $Co(OH)_2$ electrocatalyst supported on indium tin oxide (ITO) electrodes[23]. Their findings confirmed that CoOOH acts as the true catalytically active phase during the OER under alkaline conditions, demonstrating that the magnitude of the electrocatalytic enhancement is strictly dependent on the precise spatial configuration of the Au–electrocatalyst interface. Carbon-based support offers well-known advantages in electrocatalysis, including high specific surface area, excellent electrical conductivity, and robust chemical inertness[24].

Although various composites with a plasmonic effect have frequently been used to enhance OER kinetics in water-splitting systems[14,22,24,25], rechargeable Zn-air batteries require bifunctional materials capable of catalyzing both the OER and the ORR in alkaline aqueous electrolyte.

To address this challenge, we herein develop a polydopamine-derived (PDA) nitrogen-doped carbon nanostructure anchoring cobalt oxide (Co_3O_4) as a bifunctional electrocatalyst. To build the final architecture, (PDA@Co_3O_4) was systematically assembled with varying relative amounts of gold nanorods (AuNRs) through electrostatic self-assembly.

Following comprehensive structural and morphological verification, the plasmonic-assisted electrocatalysis of the resulting PDA@Co_3O_4@AuNRs heterostructures was thoroughly evaluated under both dark and near-infrared (NIR) laser illumination. Notably, our electrochemical results demonstrate that optimizing the AuNRs concentration within the heterostructure is paramount to achieving peak plasmon-enhanced OER activity,

whereas an excess of plasmonic components exerts a detrimental shielding effect on the catalytic centers. To validate the practical feasibility of this optimized heterostructure, it was integrated into a rechargeable zinc–air battery (ZAB). When evaluated under *in situ* laser irradiation, the ZAB exhibited a significant performance enhancement during both the charge and discharge processes, showcasing the immense potential of plasmon-driven energy devices. To the best of our knowledge, such synergistic implementation in ZABs, alongside the systematic elucidation of the detrimental effect of excessive AuNRs loading, has not been previously reported.

EXPERIMENTAL

Chemical and reagents

All chemical reagents were of analytical grade, purchased from Merck, and used as received without further purification. Ultrapure water (18.2 MΩ·cm) was obtained from a Milli-Q Direct water purification system.

Catalysts synthesis

Synthesis of gold nanorods (AuNRs)

AuNRs were synthesized via a seed-mediated growth method[26]. For the seed solution, 5.0 mL of 0.2 M cetyltrimethylammonium bromide (CTAB) was mixed with 5.0 mL of 0.5 mM $HAuCl_4$, followed by the rapid injection of 0.6 mL of freshly prepared, ice-cold 0.01 M $NaBH_4$. The mixture was allowed to react undisturbed at 28 °C for 30 min. The growth solution was prepared by sequentially mixing 5.0 mL of 0.2 M CTAB, 250 µL of 1 M HCl, 250 µL of 4 mM $AgNO_3$, and 5.0 mL of 1 mM $HAuCl_4$. Subsequently, 70 µL of 0.1 M ascorbic acid (AA) was introduced, and the solution was gently agitated until it became completely colorless. Finally, 12 µL of the seed solution was added, and the growth process was maintained at 30 °C for 3 h. The as-synthesized AuNRs were isolated and purified by centrifugation (7,500 rpm, 30 °C, 30 min) and resuspended in ultrapure water. This washing procedure was repeated twice to eliminate excess CTAB surfactant. The final colloidal suspension was stored at room temperature in the dark. The concentration of metallic gold was determined to be 0.37 mM based on the optical absorbance at 400 nm[27].

Synthesis of polydopamine-derived n-carbon (PDA)

The nitrogen-doped carbon (N-carbon) matrix was synthesized using polydopamine

(PDA) as the precursor[28]. Typically, 1.4 g of dopamine hydrochloride and 3.0 g of NH_4Cl were dissolved in 50 mL of ultrapure water. The pH of the solution was adjusted to 8.5 by the dropwise addition of 0.1 M KOH to initiate self-polymerization, and the mixture was continuously stirred for 24 h under ambient conditions. The resulting PDA suspension was evaporated to dryness using a rotary evaporator. The collected powder was subsequently subjected to a controlled thermal treatment at 350 °C for 3 h in air (heating rate: 5 °C·min^{-1}) to yield the final N-carbon material.

Synthesis of the PDA@Co_3O_4 hybrid matrix

The cobalt-embedded N-carbon hybrid matrix was prepared via an identical polymerization-calcination route, with the integration of 112 mg of $CoCl_2 \cdot 6H_2O$ into the initial reaction mixture containing dopamine and NH_4Cl. The pH was adjusted to 8.5 using 0.1 M KOH, and the solution was stirred for 24 h. Following solvent evaporation, the resulting cobalt-PDA composite powder was calcined at 350 °C for 3 h under an air atmosphere. This thermal process simultaneously induced the partial carbonization of the polymer matrix and the crystalline evolution of uniformly distributed Co_3O_4 nanoparticles within the N-carbon network.

Assembly of PDA@Co_3O_4@AuNRs heterostructures

Plasmonic heterostructures with varying noble metal loadings were fabricated by anchoring different volumes of the purified AuNRs onto the pre-formed hybrid matrix. The resulting composites were designated as PDA@Co_3O_4@Au100, PDA@Co_3O_4@Au50, and PDA@Co_3O_4@Au10. For PDA@Co_3O_4@Au100, 5.0 mg of the PDA@Co_3O_4 powder was dispersed in 1.0 mL of the 0.37 mM AuNRs colloidal suspension. For PDA@Co_3O_4@Au50, 5.0 mg of the matrix was suspended in a mixture of 0.5 mL of the AuNRs colloid and 0.5 mL of ultrapure water. For PDA@Co_3O_4@Au10, 5.0 mg of the matrix was treated with 0.1 mL of the AuNRs colloid combined with 0.9 mL of ultrapure water. The nominal metallic gold contents in these three heterostructures corresponded to approximately 72.9 μg (~1.44 wt.%), 36.4 μg (~0.72 wt.%), and 7.3 μg (~0.15 wt.%) of Au per 5.0 mg of the PDA@Co_3O_4 support, respectively.

Physical characterizations

UV–vis absorption spectra were recorded on a Jasco V-750 double-beam spectrophotometer. X-ray photoelectron spectroscopy (XPS) measurements were

performed using a SPECS PHOIBOS 150 MCD spectrometer. The X-ray source was Al Kα, with an excitation energy of 1,486.71 eV. High-resolution spectra were acquired in the constant energy pass mode at 30 eV, utilizing an analysis area diameter of 720 µm. The binding energies were calibrated against the adventitious C 1s peak at 284.8 eV, and data processing was conducted using the CasaXPS software package (version 2.3.16). X-ray diffraction (XRD) patterns were collected on a Bruker D8 ADVANCE diffractometer operating at 40 kV and 40 mA, utilizing Cu Kα radiation (λ = 1.5406 Å). High-resolution transmission electron microscopy (HR-TEM) images, along with scanning transmission electron microscopy-high angle annular dark-field (STEM-HAADF) imaging and energy-dispersive X-ray spectroscopy (EDS) elemental mapping, were acquired on a Thermo Scientific Talos F200i system operating at an accelerating voltage of 80 kV. Samples for TEM analysis were prepared by drop-casting the dispersed hybrids onto carbon-coated copper grids, followed by drying under ambient conditions. UV-Vis diffuse reflectance spectra were recorded using a Varian Cary 5E spectrophotometer equipped with a Praying Mantis accessory. The resulting reflectance data were converted into the Kubelka-Munk function to evaluate the optical properties of the materials and provide the experimental input for light-matter interaction modelling. Optical band gap data were estimated using the Tauc method.

Light-matter interaction modelling for LSRPA calculation

The interaction between the incident radiation and the investigated materials deposited on the electrode was evaluated using a simplified radiative transfer approach to determine the local superficial rate of photon absorption (LSRPA). The modelling procedure was based on the general principles of the radiative transfer equation (RTE), considering radiation propagation from the illumination source to the sample surface and its subsequent absorption by the materials[29,30]. The experimental illumination system consisted of a DS3-11312-110-K808F15FA-8.00W radiation source, with a nominal optical power of 8 W and a central emission wavelength of 808 +/- 10 nm. The samples investigated were modelled as circular surfaces with a diameter of 5 mm, corresponding to the geometry of the working electrode. The LSRPA was determined by integrating the absorbed spectral photon flux over the irradiation wavelength range, considering both direct photon absorption by the catalyst layer and the additional contribution arising from radiation reflected by the underlying glassy carbon electrode (GCE). Steady-state irradiation conditions were assumed, while absorption and scattering in the surrounding

media, as well as thermal emission within the investigated spectral range, were considered negligible. The model incorporates the spectral transmittance of the surrounding medium, the experimentally determined wavelength-dependent optical properties of the catalyst layer, and the spectral reflectance of the glassy carbon substrate. The LSRPA was calculated using Equation (1):

$$LSRPA(x,y) = \int_{\lambda} q_{\lambda}(x,y)\, T_m(\lambda)\, A_c(\lambda) \left(1 + \frac{R_{GC}(\lambda) T_c(\lambda)}{1 - R_{GC}(\lambda) R_c(\lambda)}\right) d\lambda$$

In Equation 1, q_λ represents the local spectral photon flux incident on the electrode surface, T_m is the spectral transmittance of the surrounding medium, and A_c, R_c and T_c correspond to the experimentally determined spectral absorptance, reflectance and transmittance of the catalyst layer, respectively. R_{GC} represents the spectral reflectance of the glassy carbon electrode. The term in brackets accounts for the additional photon absorption arising from multiple reflections between the catalyst layer and the glassy carbon electrode. The model assumes uniform optical properties, incoherent reflections, equivalent optical behavior in both propagation directions, and an optically opaque substrate (the GC electrode is considered optically opaque), while neglecting scattering losses, interference and polarization effects. These assumptions are commonly adopted in systems involving supported catalysts[31]. The resulting LSRPA distributions were represented as two-dimensional spatial maps and expressed in Einstein $cm^{-2} \cdot s^{-1}$.

Electrochemical measurements

Electrochemical measurements were performed on a BioLogic VMP-3e potentiostat/galvanostat utilizing a standard three-electrode cell configuration. A platinum wire and an Ag/AgCl (3 M KCl) electrode served as the counter and reference electrodes, respectively. A glassy carbon disk electrode (GCE, 5 mm in diameter, geometric area: 0.196 cm^2, AFE3T050GC, Pine Research Instrumentation) was employed as the working electrode substrate. All electrochemical experiments were conducted in an aqueous 0.1 M KOH supporting electrolyte.

Rotating disk electrode (RDE) and rotating-ring disk electrode (RRDE) analysis for the OER and ORR were executed using a modulated speed rotator (AFMSRCE, Pine Research Instrumentation) at a constant rotation speed of 1,600 rpm. The working electrodes were fabricated by dispersing 5.0 mg of the respective N-carbon material

(PDA, PDA@Co_3O_4, PDA@Co_3O_4@Au100, PDA@Co_3O_4@Au50, or PDA@Co_3O_4@Au10) in a mixture of ultrapure water, isopropanol, and 5 wt.% Nafion solution to form a homogeneous 5.0 mg·mL^{-1} catalyst ink. A 25 µL aliquot of this ink was drop-cast onto the polished GCE surface (yielding a dry support mass loading of ~0.64 mg·cm^{-2} or 0.125 mg of PDA-based matrix) and dried overnight at 4 °C. The nominal gold mass loadings on the GCE for the Au100, Au50, and Au10 heterostructures were calculated to be approximately 1.82, 0.91, and 0.18 µg, respectively. All measured potentials were converted and reported against the reversible hydrogen electrode (RHE) using the Nernst equation: $E_{RHE} = E_{Ag/AgCl} + E°_{Ag/AgCl} + 0.059 \times pH$

For the photo-electrochemical, the modified GCEs were irradiated using a fiber-coupled near-infrared (NIR) diode laser system (PSU-W-FC, 808 ± 5 nm, SMA 905 coupling) with an adjustable power density ranging from 0.03 to 0.18 mW·cm^{-2}[32].

Zinc-air battery evaluation

Liquid-state Zn-air batteries (ZABs) were assembled in a home-made configuration and tested using a BioLogic BCS-810 battery cycler. The air cathodes (positive electrodes) were prepared by blending 45 µL of the catalyst ink (15 mg·mL^{-1} in water/isopropanol; 0.675 mg of active hybrid) with 5.0 µL of a 5 wt.% Nafion solution. This mixture was drop-cast stepwise onto a carbon cloth gas diffusion layer (GDL, ELAT LT1400W, Fuel Cells Store) to achieve a uniform catalyst loading over a geometric contact area of 0.63 cm^2. A polished Zinc plate served as the anode, and a 6.0 M KOH aqueous solution (1.0 mL) was employed as the liquid electrolyte. Nickel meshes were utilized as current collectors for both electrodes. Galvanostatic discharge profiles were recorded at continuous current conditions of ±0.1, ±5, ±10 and ±20 mA under ambient air. To conduct these measurements, an identical home-made cell to those previously utilized in several studies was employed[33]. However, in this work, the NIR laser light was directed onto the backside of the air electrode.

RESULTS AND DISCUSSION

Figure 1A shows a schematic representation of the synthesis route for the PDA-based N-carbon material containing cobalt oxide and gold nanorods (AuNRs) (see Supplementary Figure 1 for more details). Firstly, in order to obtain nitrogen-enriched carbonaceous materials, dopamine was polymerized to yield polydopamine (PDA) in a slightly alkaline

aqueous medium (pH 8.5) in the presence of cobalt (II) ions for 24 h. Subsequently, the resulting PDA with trapped cobalt ions was dried and thermally treated to induce carbonization (see experimental section for further details). Pristine PDA without cobalt (II) ions was also prepared as a control sample. Finally, appropriate mass of the PDA@Co_3O_4 powder was dispersed in AuNRs colloidal suspension to obtain different PDA@Co_3O_4@Au materials (see experimental section for further details).

The structural features, crystalline phases, and textural properties of the resulting carbonized PDA with and without cobalt, denoted as PDA@Co_3O_4 and PDA, respectively, were initially evaluated by X-ray powder diffraction (XRPD). As shown in Supplementary Figure 2A, the pristine PDA sample exhibits a broad band in the 2θ range of 15°-35° along with a distinguishable peak at approximately 26°, indexed as the (200) plane. This profile confirms the predominantly amorphous nature of the carbonized polydopamine matrix with incipient short-range graphitic stacking[34]. In contrast, the XRPD pattern of the PDA@Co_3O_4 composite displays well-defined, sharp diffraction peaks at 2θ values of 19.0°, 31.3°, 36.8°, 44.8°, 59.4°, and 65.2°. These reflections correspond perfectly to the (220), (311), (400), (422), (511), and (440) crystallographic planes of the standard cubic spinel structure of Co_3O_4 (space group *Fd3m*), in accordance with JCPDS No. 42-1467. This transformation demonstrates that the thermal treatment at 350 °C successfully drove the effective oxidation and crystallization of the coordinated Co^{2+} ions into highly crystalline Co_3O_4 nanoparticles embedded within the carbonaceous matrix[35].

The optical properties of the PDA@Co_3O_4 were evaluated via UV-Visible-NIR spectroscopy. As shown in Supplementary Figure 2B, the absorption spectrum of PDA@Co_3O_4 preserves the characteristic electronic transitions of commercial Co_3O_4, while exhibiting a general increase in absorbance across the entire wavelength range (250-2,000 nm) due to the presence of the polydopamine-derived carbon framework.

The morphological evolution of the materials was examined via transmission electron microscopy (TEM), as displayed in Figures 1B-1D. The pristine PDA [Figure 1B] exhibits smooth, sheet-like carbon structures. Upon calcination, the PDA@Co_3O_4 sample [Figure 1C] displays distinct granular and polyhedral networks, verifying the

homogeneous nucleation and deposition of the cobalt oxide nanoparticles over the carbonaceous support. Finally, after the incorporation of the metallic promoter [Figure 1D], the characteristic elongated morphologies of the gold nanorods (AuNRs) can be clearly observed well-dispersed and successfully anchored onto the Co_3O_4/N-carbon heterostructure, showing no signs of aggregation.

Next, AuNRs were synthesized via a traditional seed-mediated growth method[32], and the resulting Au colloidal dispersion exhibited the two characteristic surface plasmon resonance (SPR) bands observable by UV-visible spectroscopy [Supplementary Figure 3A]. The transverse SPR band appears at ca. 515 nm, corresponding to the collective oscillation of conduction electrons along the short axis of the AuNRs, while the longitudinal SPR band is observed at 750 nm, associated with the electron oscillation along the long axis. The strong, sharp, and well-defined nature of the longitudinal peak suggests the successful formation of highly monodisperse rod-like gold nanostructures with an aspect ratio of ca. 3.6. The TEM image of the resulting AuNRs [Supplementary Figure 3B] clearly confirms the structural and morphological uniformity indicated by the optical measurements, showing well-defined, isolated nanorods without significant shape impurities.

Subsequently, powdered PDA@Co_3O_4 was suspended in an aqueous colloidal dispersion of the synthesized CTAB-capped AuNRs to generate the final PDA@Co_3O_4@AuNRs composite via a simple, one-pot electrostatic self-assembly approach (see section 3.6 for further details). The formation of this plasmonic nanostructure was systematically monitored by Zeta-Potential (ZP) measurements, as summarized in Supplementary Table 1. The ZP of the pristine PDA suspended in pure water was highly negative (ca. -40 mV)[36] , which is expected due to the deprotonation of its abundant catechol (phenolic hydroxyl) and amine groups at neutral pH, creating a net negative surface charge density. In contrast, the PDA@Co_3O_4 composite exhibited a nearly neutral, slightly negative ZP value of ca. -0.2 mV under identical conditions[37,38]. On the other hand, the CTAB-capped AuNRs possessed a strongly positive ZP (ca. +30 mV) because the surfactant forms a bilayer on the gold surface with its cationic trimethylammonium headgroups exposed outward, ensuring high electrostatic stabilization[39]. Upon the immobilization of the AuNRs onto the surface of the PDA@Co_3O_4 composite, the ZP of the resulting hybrid structure shifted significantly to +57.8 mV. This clear charge reversal toward a

high positive value confirms the successful anchoring of the AuNRs and the subsequent exposure of their outer quaternary ammonium headgroups.

The structural integration was further supported by TEM imaging of the PDA@Co_3O_4@AuNRs composite [Figure 1D], which confirms the coexistence and homogeneous distribution of the AuNRs within the polyhedral network of the PDA@Co_3O_4 support, yielding a well-defined hierarchical architecture. Furthermore, the high-angle annular dark-field scanning transmission electron microscopy (HAADF-STEM) image [Figure 1E] and its corresponding energy-dispersive X-ray spectroscopy (EDS) elemental mapping analysis [Figures 1F-J] reveal a uniform distribution of all constituent elements across the hybrid matrix. Specifically, the strong co-localization of cobalt [Figure 1F] with oxygen [Figure 1J] unambiguously demonstrates the formation of the cobalt oxide domains anchored to the nitrogen-rich PDA framework [Figures 1G and 1I], while the gold signal [Figure 1H] clearly traces the spatial distribution of the exposed AuNRs on the surface. Supplementary Figures 4 and 5 provide additional reference HAADF-STEM images and EDS mapping analysis for the pristine PDA and the intermediate PDA@Co_3O_4 sample, respectively, validating the sequential elemental and compositional integration of the final hybrid catalyst.

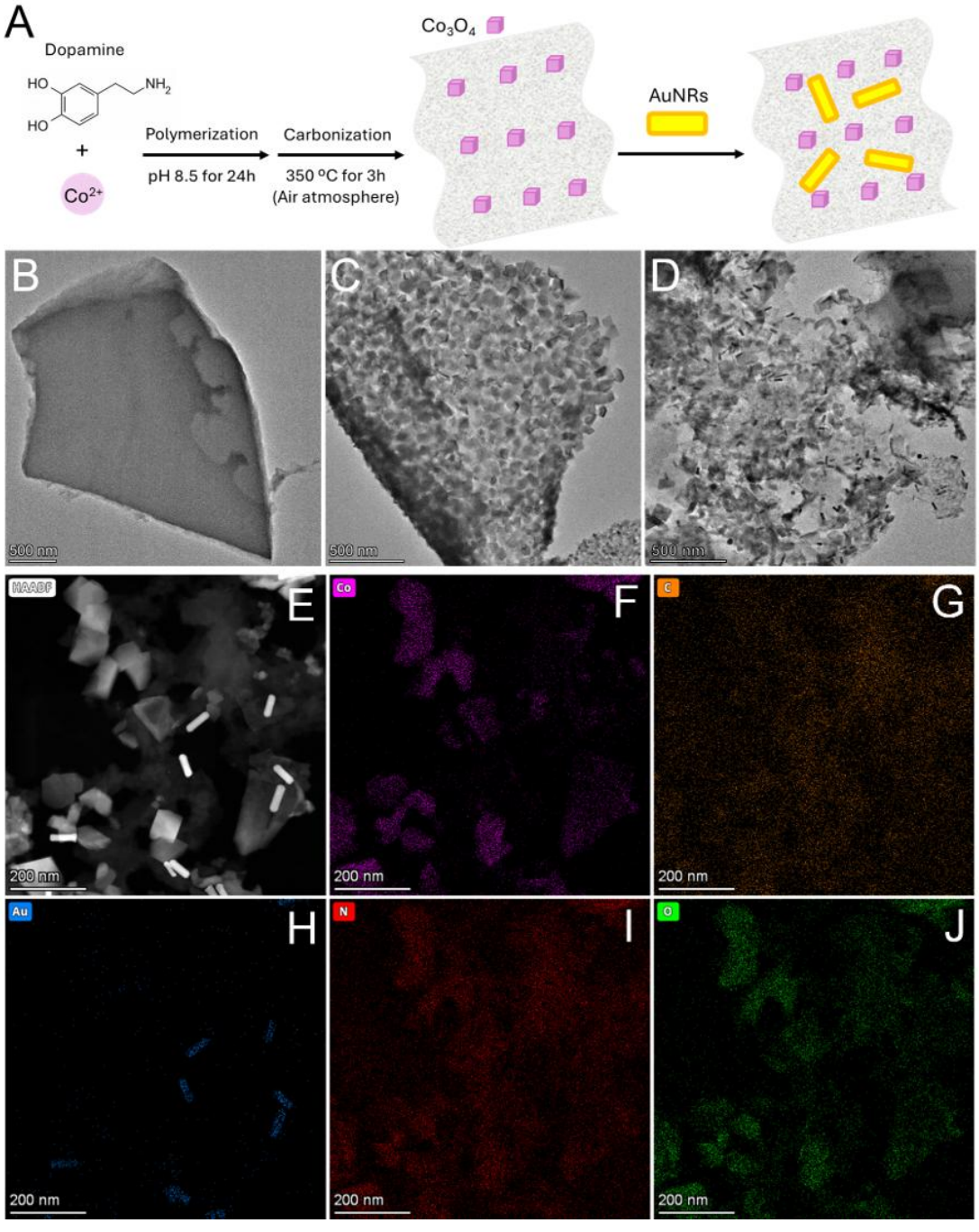


Figure 1. (A) Schematic representation of the synthesis of the PDA@Co_3O_4@AuNRs nanocomposite described in this work; (B-D) TEM images of the carbonized PDA, carbonized PDA@Co_3O_4 and PDA@Co_3O_4@Au100 samples, respectively; (E) HAADF-STEM image and (F-J) EDS elemental mapping images (with Co, C, Au, N, and O distribution) of the same PDA@Co_3O_4@Au100 sample.

To attain a more detailed characterization of the resulting nanostructures, the surface chemical composition and electronic states were assessed by XPS. Supplementary Figure

6 compares the XPS survey spectra of PDA, PDA@Co_3O_4, and PDA@Co_3O_4@Au100. The survey spectrum of carbonized PDA matrix predominantly displays the characteristic peaks corresponding to C 1s, N 1s and O 1s, which are highly typical of the core elements in dopamine-derived polymeric frameworks[40]. Upon cobalt incorporation and calcination (PDA@Co_3O_4), an additional photoelectron line emerges corresponding to Co 2p, accompanied by a notable increase in the relative intensity of the O 1s peak, which fundamentally confirms the successful *in situ* formation of the Co_3O_4 phase within the nitrogen-doped carbon matrix. Furthermore, the survey spectrum of the fully assembled PDA@Co_3O_4@Au100 nanostructure exhibits additional well-defined signals attributed to Au 4f, successfully validating the electrostatic self-assembly of the AuNRs on the PDA@Co_3O_4 surface. This gradual appearance of specific elemental peaks in tandem with the sequential incorporation of Co_3O_4 and AuNRs further supports the stepwise functionalization strategy and confirms the multi-component nature of the final hybrid catalyst.

Figure 2 shows the deconvoluted HR XPS spectra of PDA, PDA@Co_3O_4 and PDA@Co_3O_4@Au100 at the C 1s, N 1s, O 1s, Co 2p and Au 4f core levels. The C 1s HR spectrum of pristine PDA control [Figure 2A] displays three deconvoluted components attributed to C-C/C=C (284.8 eV), C-N/C-O (285.8 eV), and C=O (288.2 eV), which are characteristic of the residual catechol and amine moieties within the carbonized framework[41]. The deconvoluted N 1s HR spectrum [Figure 2D] reveals two main components located at 397.1 and 399.5 eV, corresponding to pyridinic and graphitic/pyrrolic nitrogen species integrated into the nitrogen-rich matrix[42]. Additionally, the O 1s HR spectrum of pristine PDA [Figure 2G] exhibits a major asymmetric profile centered at 530.85 eV, which resolves into two distinct chemical states assigned to carbonyl (530.2 eV) and phenolic/hydroxyl (531.5 eV) oxygen groups, thereby confirming the characteristic organic functional platform of the polymer matrix[43].

For the PDA@Co_3O_4 sample, the HR profiles of C 1s [Figure 2B], N 1s [Figure 2E], and O 1s [Figure 2H] retain chemical environments analogous to pristine PDA framework. However, they exhibit perceptible binding energy shifts and variations in relative intensities, which suggests an intimate electronic interaction between the N-doped carbon support and the hosted cobalt oxide phase. Notably, the O 1s spectrum of

PDA@Co_3O_4 reveals a highly prominent deconvoluted peak at 531.3 eV, strictly attributed to metal-oxygen bonds (Co-O) of the oxide lattice[44]. Furthermore, the Co 2p HR spectrum of PDA@Co_3O_4 [Figure 2K] confirms the formation of the spinel structure, displaying the characteristic Co $2p_{3/2}$ and Co $2p_{1/2}$ core levels at 780.0 and 795.5 eV, respectively. The spin-orbit splitting ($\Delta E \sim 15.5$ eV) along with the absence of prominent satellite features are indicative of the coexistence of mixed Co^{2+}/Co^{3+} valence states typical of Co_3O_4.

Regarding the final PDA@Co_3O_4@Au100 plasmonic hybrid, the C 1s [Figure 2C], O 1s [Figure 2I] and Co 2p [Figure 2L] HR XPS spectra display subtle binding energy shifts compared to their precursors. These modifications point to an enhanced electron delocalization and interfacial charge redistribution driven by the anchoring of the plasmonic domains. Notably, the N 1s spectrum [Figure 2F] displays a newly emerged component at 402.0 eV, which is unambiguously attributed to the quaternary ammonium nitrogen (N^+) of the CTAB surfactant bilayer capping the AuNRs, thereby confirming their sSupplementary Table urface immobilization[45]. Moreover, the Au 4f HR spectrum [Figure 2O] resolves into two sharp, symmetric peaks at 82.7 eV (Au $4f_{7/2}$) and 86.3 eV (Au $4f_{5/2}$), confirming the metallic nature (Au^0) of the nanorods. Notably, the PDA@Co_3O_4@Au100 hybrid displays a substantial downshift of ~1.4 eV relative to the pristine AuNRs@CTAB precursor, whose Au $4f_{7/2}$ and Au $4f_{5/2}$ peaks emerge at 84.1 eV and 87.7 eV, respectively, consistent with prior studies[44,45]. Supplementary Figure 7 compares the Au 4f region for both samples[45,46]. A similar shift was observed before for TiO_2-Au NPs heterojunction, which was explained as due to electron transfers from TiO_2 to Au without any chemical bonding between Au and TiO_2, leading to the increment in the charge density on the surface of Au NPs[46]. Furthermore, this pronounced binding energy shift toward lower eV serves as strong evidence of a substantial interfacial electron transfer from the surrounding semiconductor/carbon matrix to the plasmonic metallic domains, a highly beneficial feature for modulating the local electron density during electrocatalysis.

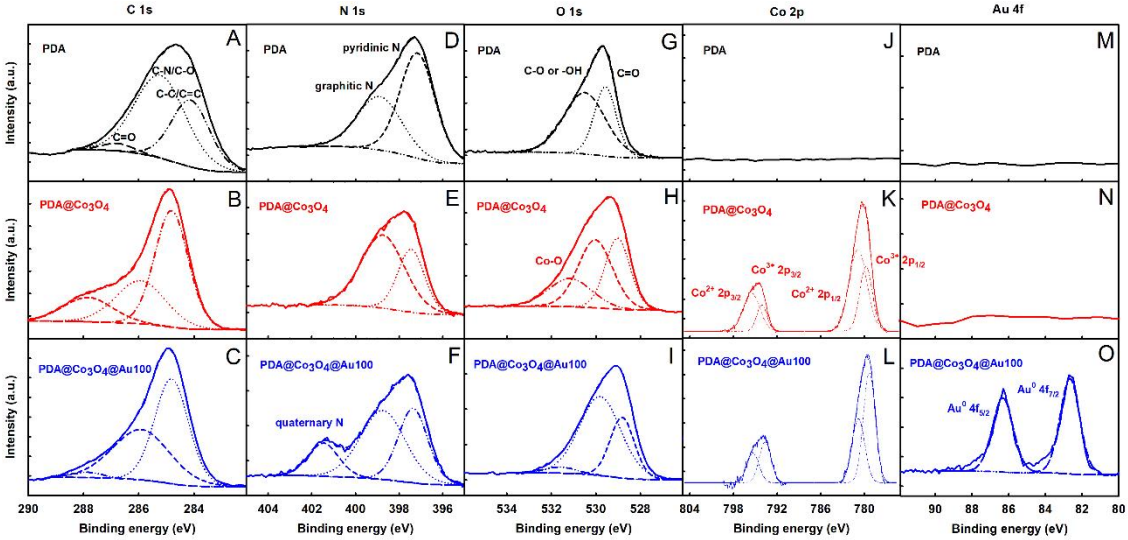


Figure 2. High-Resolution XPS spectra of (A-C) C1s; (D-F) N1s; (G-I) O1s; (J-L) Co 2p and (M-O) Au 4f for PDA, carbonized PDA@Co_3O_4 and PDA@Co_3O_4@Au100 samples.

In this regard, deconvolution of the Co $2p_{3/2}$ and Co $2p_{1/2}$ peaks was executed to evaluate the Co^{3+} and Co^{2+} concentrations in both PDA@Co_3O_4@Au100 and PDA@Co_3O_4. As illustrated in Figure 2, the peak intensities Co^{2+}/Co^{3+} ratio is diminished upon the inclusion of AuNRs in the composite structure, from 1.26 to 0.58, confirming the higher amount of Co^{3+} on the composite surface when AuNRs were incorporated to the composite. This outcome can be rationalized by the negative shift detected in the Au $4f_{7/2}$ and Au $4f_{5/2}$ states, resulting from electrons transfer from Co_3O_4 to Au that promote the oxidation of Co^{2+} to Co^{3+}.

The spatial distribution of the LSRPA was evaluated to assess the wavelength-dependent photon absorption behavior of the investigated materials [Figure 3]. Initially, the AuNRs system was analyzed under a simulated irradiation of 750, 800 and 850 nm, respectively [Figure 3A-C]. The highest mean LSRPA was obtained at 800 nm (7.98×10^{-9} Einstein cm^{-2} s^{-1}), approximately 6.7 and 5.9 times higher than those determined at 750 nm (1.18×10^{-9} Einstein cm^{-2} s^{-1}) and 850 nm (1.34×10^{-9} Einstein cm^{-2} s^{-1}), respectively. This pronounced wavelength dependence is in line with a well-defined absorption maximum around 800 nm, consistent with previous reports describing localized surface plasmon resonance (LSPR) in Au nanostructures within the near-infrared region[47]. More

importantly, the comparative analysis of AuNRs, PDA@Co_3O_4 and PDA@Co_3O_4@Au [Figure 3D-F], revealed substantial differences in their photon absorption behavior, with mean LSRPA values of 2.62 × 10^{-9}, 2.99 × 10^{-8} and 3.11× 10^{-8} Einstein cm^{-2} s^{-1}, respectively. The PDA@Co_3O_4@Au sample exhibited an approximately 11.9-fold higher LSRPA than AuNR and a 4.2% increase compared with the PDA@Co_3O_4 sample. These results demonstrate that the Co_3O_4-containing component dominates the overall photon absorption within the irradiation conditions investigated, while the incorporation of AuNR provides only a marginal additional contribution. This limited enhancement suggests that the optical response of the composite is primarily governed by the oxide-containing structure, with AuNR incorporation having a relatively minor influence on the overall photon absorption rate. Nevertheless, the modest increase in LSRPA does not necessarily exclude other potential contributions of AuNR to photocatalytic performance, particularly those associated with interfacial charge transfer, charge-carrier separation, or plasmon-mediated processes, which cannot be established from photon absorption analysis alone[48].

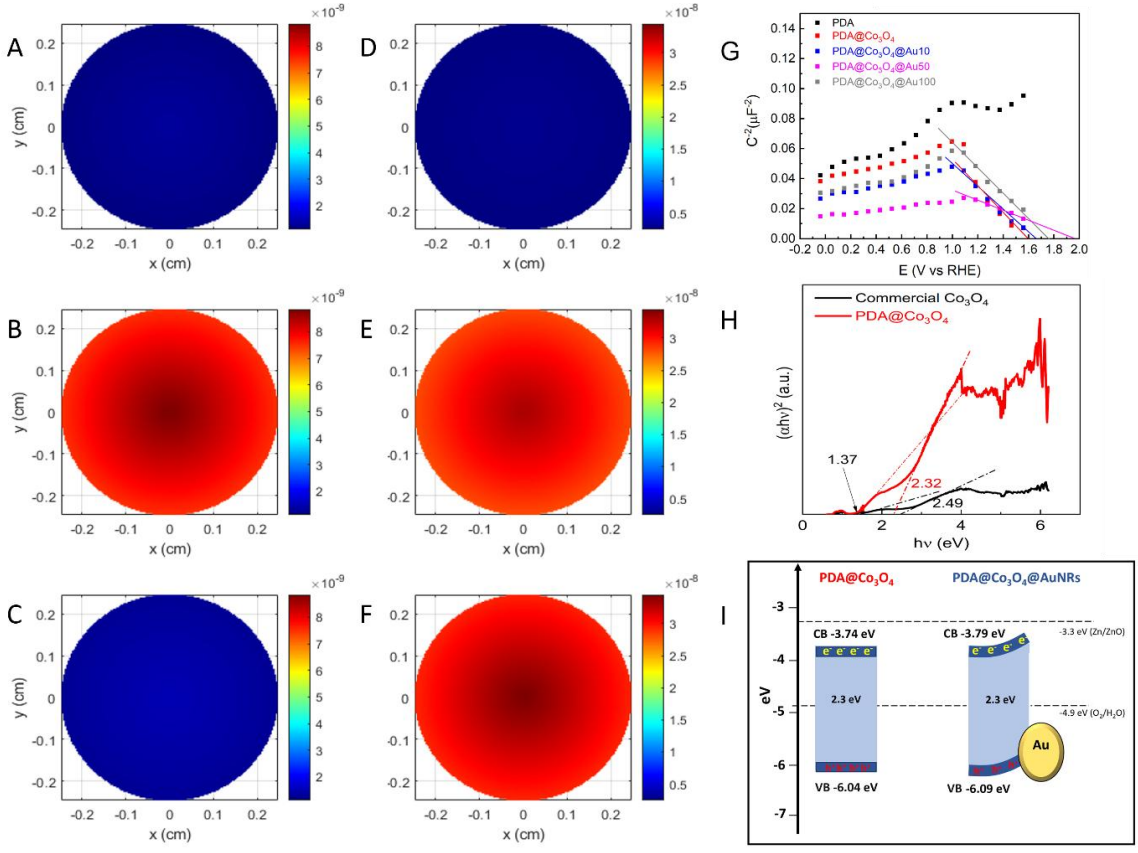


Figure 3. LSRPA for (A-C) AuNR under irradiation at 750, 800 and 850 nm, respectively, and (D-F) AuNRs, PDA@Co_3O_4 and the PDA@Co_3O_4@Au, respectively. Different colour scales were used for panels A-C and D-F to facilitate visualization of the LSRPA distributions. Data are expressed in Einstein cm^{-2} s^{-1}; (G) Mott-Schottky (3 k); (H) tauc plots of the PDA@Co_3O_4 synthesized and Co_3O_4 commercial as a reference; (I) Band structure scheme for PDA@Co_3O_4 and the PDA@Co_3O_4@Au in dark conditions.

The electronic features of the representative synthesized catalysts (PDA@Co_3O_4 and PDA@Co_3O_4@Au) were probed via electrochemical characterization. Figure 3G shows the Mott–Schottky (M–S) plots of PDA, PDA@Co_3O_4, PDA@Co_3O_4@Au10 and PDA@Co_3O_4@Au100, displaying a well-defined linear regime between $1/C^2$ and the applied potential over an extended potential window. This behavior confirms that the measured capacitance is governed by the space-charge layer, thereby substantiating the validity of the M–S framework for these systems. The negative slopes recorded across all samples corroborate their characteristic *p*-type semiconducting nature, in which holes

serve as majority charge carriers. Consequently, the flat-band potential derived from the intercept allows for the estimation of the valence band edge. Furthermore, the overall $1/C^2$ versus E (V *vs.* RHE) profile for PDA@Co_3O_4 closely aligns with literature report[49]. Electrochemical characterization via Mott–Schottky analysis reveals a progressive anodic shift of the flat-band potential (E_{fb}) toward more positive values upon the functionalization of the PDA@Co_3O_4 heterostructure with AuNRs. This behavior is primarily governed by the formation of a metal–semiconductor junction and the subsequent thermodynamic equilibration via Fermi level alignment: owing to the high work function of metallic gold relative to the Co_3O_4 semiconductor and polydopamine matrix, a net interfacial electron transfer occurs from the host composite toward the Au nanoarchitectures. This redistribution of charge modulates the electrostatic potential drop across the space-charge region, thereby systematically altering the degree of band bending required to attain the flat-band condition, passing from 1.60 V *vs.* RHE for the PDA@Co_3O_4 to 1.65 V *vs.* RHE for the PDA@Co_3O_4@Au10 and finally to 1.75 V *vs.* RHE for the PDA@Co_3O_4@Au100. Notably, the magnitude of this positive shift exhibits a direct dependence on the incorporated gold loading; increasing Au concentration enhances the interfacial contact site density, maximizes electron-trapping capability, and induces a more pronounced interfacial dipole polarization, which translates into a significantly greater anodic displacement of E_{fb} and promotes more efficient charge separation.

The determination of the optical bandgap using the Tauc plot correlates directly with the E_{fb} obtained by the Mott-Schottky method. This synergy not only allows the alignment of the conduction and valence energy levels with respect to the thermodynamic reaction potentials but also enables a comparison of the nature of the electronic transition with the predominant type of doping. Figure 3H shows the Tauc plot obtained from UV-vis diffuse reflectance spectra [Supplementary Figure 2B], which reveals the presence of three distinct optical band gaps for both the commercial cobalt oxide and the synthesized PDA@Co_3O_4 composite. While both materials exhibit two lower-energy electronic transitions centered at 1.37 eV and 0.90 eV, a discernible shift is observed in the highest-

energy transition, which decreases from 2.49 eV in the commercial reference to 2.32 eV in PDA@Co_3O_4. In mixed-valence spinel systems ($Co^{2+}[Co^{3+}]_2O_4$), multiple absorption edges are typically governed by ligand-to-metal charge transfers alongside intra-ionic d-d crystal field transitions, as it has been reported frequently. The remarkable narrowing of the highest-energy band gap (from 2.49 eV to 2.32 eV) can be directly rationalized by deviations in stoichiometry and cation distribution between the commercial benchmark and our synthesized sample. Variations in the relative Co^{2+}/Co^{3+} ratio, coupled with surface oxygen vacancies and coordination alterations induced during the synthesis and polydopamine interfacial hybridization, may perturb the local octahedral/tetrahedral ligand field. This should create sub-band defect states near the band edges, effectively reducing the energy required for fundamental interband charge transfer while preserving the deeper intra-band d-d transition energies at 1.37 eV and 0.90 eV[50].

Figure 3I shows the band alignment and electronic structure derived from Mott-Schottky and Tauc plot analyses, which reveals that while the optical band gap remains constant at 2.32 eV, indicating that Au incorporation preserves the fundamental interband electronic transitions of Co_3O_4,the absolute energy levels undergo a rigid downward shift of 0.05 eV from PDA@Co_3O_4 (E_{CB} = -3.74 eV and E_{VB} = -6.04 eV *vs.* vacuum) to PDA@Co_3O_4@Au10 (E_{CB} = -3.79 eV and E_{VB} = -6.09 eV *vs.* vacuum). This energetic displacement is governed by the establishment of a Schottky-type junction at the metal-semiconductor interface. Upon intimate contact, spontaneous electron transfer occurs from Co_3O_4 through the polydopamine layer into the Au nanoparticles to equilibrate the Fermi levels, generating an interfacial dipole and local band bending within the space charge layer that stabilizes the overall band positions by 50 meV. Consequently, under photoexcitation, photogenerated electrons in the conduction band are thermodynamically driven downhill to accumulate within the Au nanoparticles, which serve as efficient electron sinks, while photogenerated holes remain isolated in the valence band, thereby drastically suppressing charge carrier recombination and facilitating directional charge transfer for enhanced catalytic performance. Furthermore, with the valence band positioned at -6.09 eV, this configuration provides an ample thermodynamic

overpotential to drive water oxidation via the O_2/OH^- redox couple located at -4.83 eV *vs.* vacuum in alkaline media, confirming the suitability of the heterostructure for highly efficient oxygen redactions[51].

OER and ORR analysis

To evaluate the electrocatalytic performance of the prepared catalysts for the oxygen evolution reaction (OER), linear sweep voltammetry (LSV) measurements were performed in alkaline media, both in the dark and under NIR irradiation. As shown in Figure 4A, pristine PDA and AuNRs exhibit negligible catalytic response in both environments, confirming their lack of direct contribution to catalyzing the OER. Conversely, the PDA@Co_3O_4 sample displays moderate catalytic current, requiring a higher overpotential to reach a current density of 10 mA cm^{-2}, taken as a conventional reference (J_{10}). Remarkably, the ternary PDA@Co_3O_4@Au10 nanocomposite showcases a progressive and substantial enhancement in current density under dark conditions, coupled with a prominent negative shift in the onset potential. This enhancement in electrocatalytic activity in the dark can be attributed to the incorporation of AuNRs into the heterostructure, which induces a net negative surface charge and increases the concentration of surface Co^{3+} ions, as confirmed by XPS measurements, thereby multiplying the number of available active sites for the OER.

When PDA@Co_3O_4 and PDA@Co_3O_4@Au10 materials are irradiated with NIR light, an increase in catalytic activity is observed in both cases, driven by the formation of new charge carriers, electrons (e-) and holes (h+), resulting from an electronic transition from the valence band to the conduction band within the semiconductor. However, irradiation of the material containing AuNRs gives rise to a plasmonic effect that increases the number of charge carriers that facilitate the OER, in this case, holes.

Figure 4B investigates the impact of the spatial loading and density of AuNRs on the PDA@Co_3O_4 surface. In dark conditions, a volcano-type trend is observed: while moderate incorporation (Au10) optimizes performance, an excessive gold coverage

(Au50 and Au100) leads to a severe decline in OER activity. A similar behavior has been already found for Si/$Co_3O_4$5/Au composites, a lower Au content exhibited a higher photocurrent density, which was attributed to the best dispersion of AuNPs onto Co_3O_4 supporting layer[52]. Furthermore, this detrimental effect stems from the geometric blocking of the Co_3O_4 catalytic active sites. When irradiated, a similar situation is obtained, although in this case both Au10 and Au50 exceeds the catalytic activity of the PDA@Co_3O_4. Therefore, the PDA@Co_3O_4@Au10 sample balances the critical trade-off between electrocatalytic surface exposure and plasmonic enhancement.

To gain deeper insights into these reaction kinetics and evaluate the underlying charge-transfer mechanisms under excitation, Tafel plots were derived from the polarization curves under both dark and NIR-illuminated conditions [Supplementary Figure 8A], with the corresponding electrochemical parameters summarized in Supplementary Table 2. Under dark conditions, the pristine PDA@ Co_3O_4 exhibits a Tafel slope of 64.3 $mV \cdot dec^{-1}$ and an onset potential of 1.58 V *vs.* RHE. Upon the incorporation of a controlled amount of gold nanorods in the PDA@Co_3O_4@Au10 sample, the Tafel slope shifts slightly to 71.6 $mV \cdot dec^{-1}$, which can be attributed to the partial geometric coverage of the highly active cobalt sites. Interestingly, further increasing the gold loading down to PDA@Co_3O_4@Au100 lowers the dark Tafel slope to 54.2 $mV \cdot dec^{-1}$ but severely penalizes the onset potential up to 1.60 V *vs.* RHE, indicating that excessive metallic gold dominates the baseline conductivity but restricts the thermodynamic onset of the oxygen evolution reactions.

Crucially, the true superiority and synergistic potential of the electrocatalysts are unlocked under near-infrared (NIR) laser irradiation [Supplementary Figure 8B]. For the gold-free PDA@Co_3O_4 sample, the Tafel slope (65.3 $mV \cdot dec^{-1}$) and onset potential (1.58 V) remain virtually unaltered, confirming its lack of plasmonic response. In sharp contrast, all Au-containing heterostructures experience a dramatic reduction in their Tafel slopes and a concomitant negative shift in their onset potentials under NIR excitation. Most notably, the PDA@Co_3O_4@Au10 nanocomposite achieves a remarkable drop in its

Tafel slope, plummeting from 71.6 to an outstanding minimum of 51.7 $mV \cdot dec^{-1}$, accompanied by the lowest onset potential of 1.53 V *vs.* RHE. This profound kinetic acceleration directly confirms that the optimal distribution of gold nanorods in the Au10 configuration maximizes the localized surface plasmon resonance (LSPR) benefits. The efficient generation and subsequent injection of plasmonic hot-carriers into the cobalt active sites, working in tandem with the localized photothermal heat dissipation, significantly decreases the activation energy barrier for the rate-determining step in the OER pathway.

In complete agreement with these kinetic trends, upon near-infrared (NIR) laser irradiation (solid lines in Figures 4A and 4B), all Au-containing heterostructures exhibit an immediate current density upshift and a lower overpotential compared to their dark counterparts. This behavior is fundamentally validated by the chronopotentiometric transient profiles recorded under chopped NIR light illumination at a fixed current density of +10 $mA \cdot cm^{-2}$ [Figure 4C]. For the pristine PDA@Co_3O_4 baseline (red line), a small downshift (~5 mV) was observed when irradiated with NIR light, confirming that the semiconductor absorbs this radiation favoring the transition of electron from VB to CB and thus, generating extra charge carriers that facilitates the OER. However, this curve suffers from progressive anodic deactivation (potential increase over time). In stark contrast, PDA@Co_3O_4@Au10 exhibits sharp, highly reversible potential drops (photovoltage generation of ~20 mV) exactly synchronized with the laser 'on' cycles. This rapid response provides direct, real-time evidence of the localized surface plasmon resonance (LSPR) effect, wherein hot-hole injection into the Co_3O_4 valance bandlower the activation energy barrier for OER intermediates.

To complement the anodic investigation, the cathodic oxygen reduction reaction (ORR) capability was evaluated using a rotating ring-disk electrode (RRDE). As displayed in Figure 4D, PDA@Co_3O_4@Au10 does not significantly improve the performance of gold-free counterpart, although a higher ORR limiting current density (-3.2 $mA \cdot cm^{-2}$ *vs.* -2.5 $mA \cdot cm^{-2}$ at 0.0 V *vs.* RHE) and a more positive half-wave potential ($E_{1/2}$) was

obtained. The low ring current density (J_{ring}) further verifies a clean, efficient four-electron ($4e^-$) pathway with minimal peroxide generation for PDA@Co_3O_4@Au10 under NIR radiation, as it is displayed in Supplementary Figure 9.

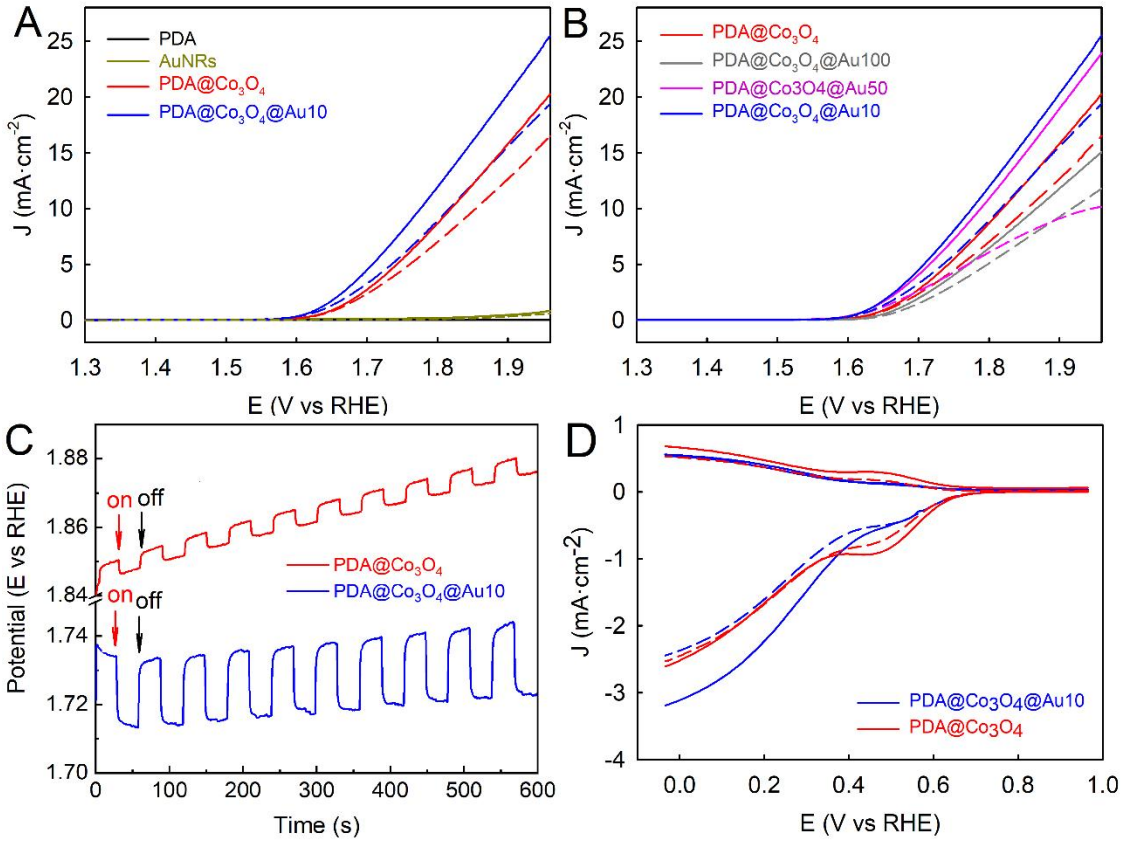


Figure 4. Electrochemical and photo-electrochemical characterization of the prepared catalysts: (A, B) Linear sweep voltammetry (LSV) curves obtained under dark conditions (dashed lines) and under near-infrared (NIR) laser irradiation (solid lines) for the different samples; (C) Chrono-potentiometric transient curves (potential *vs.* time) during chopped light illumination (on/off cycles) and (D) rotating ring-disk electrode (RRDE) voltammograms of PDA@Co_3O_4 and PDA@Co_3O_4@Au10.

These results demonstrate that the PDA@Co_3O_4@Au10 plasmonic heterostructure functions as an outstanding, high-performance bifunctional electrocatalyst optimized for zinc-air battery configurations.

To unveil the mechanisms driving the boosted electrocatalytic activity of the AuNRs-

based composite, the electrochemically active surface area (ECSA) was quantified. The double-layer capacitance C_{dl} was extracted via cyclic voltammetry in the non-Faradaic region [Supplementary Figure 10A-E]. Linear regression of the capacitive currents as a function of the scan rate [Supplementary Figure 10F] yielded C_{dl} values of 0.188, 0.204, 0.099, and 0.117 $mF \cdot cm^{-2}$ for PDA@Co_3O_4 Dark, PDA@Co_3O_4 Light, PDA@Co_3O_4@Au10 Dark, and PDA@Co_3O_4@Au10 Light, respectively. Remarkably, Au decoration decreased the C_{dl} values relative to bare PDA@Co_3O_4. This demonstrates that the peerless electrocatalytic performance of PDA@Co_3O_4@Au10 stems from enhanced intrinsic catalytic activity and optimized charge-transfer kinetics, rather than physical surface area enlargement or an increased density of catalytically active sites.

ZABs Measurements

After demonstrating the catalytic activity of the analyzed materials, we incorporated them into a gas diffusion layer (GDL) via drop-casting to prepare air electrodes, which were subsequently tested in Zn–air batteries (ZABs) both in the dark and under NIR laser radiation projected onto the electrode. The operational mechanism of the plasmonic ZAB is schematically illustrated in Figure 5G. First, polarization curves were recorded for ZABs featuring air electrodes based on PDA@Co_3O_4 and PDA@ Co_3O_4@Au10, demonstrating superior power density and catalytic performance for the PDA@ Co_3O_4@Au10 configuration, both under dark and under laser irradiation conditions [Figure 5A]. Under dark conditions, the zinc-air battery (ZAB) equipped with PDA@Co_3O_4@Au10 exhibits significant electrochemical improvements over the PDA@Co_3O_4 system in both discharge and charge processes. Laser irradiation further enhances these metrics, reaching for PDA@Co_3O_4@Au10 93.0 mA and 76.2 mA during discharge and charge, respectively. Furthermore, with the PDA@Co_3O_4@Au10 configuration, a higher power density of 84.1 $mW \cdot cm^{-2}$ was achieved, compared to the 62.9 $mW \cdot cm^{-2}$ obtained with PDA@Co_3O_4. Meanwhile, under dark conditions, the values were lower, at 54.7 and 36.9 $mW \cdot cm^{-2}$, respectively [Figure 5B].

Subsequently, galvanostatic charge-discharge cycling was performed on the batteries

utilizing PDA@Co_3O_4@Au10 as the catalyst to compare their performance with and without laser irradiation on the positive electrode. Figure 5C illustrates 20 consecutive charge/discharge cycles conducted at ±10 mA, where the first 10 cycles were performed under laser irradiation of the positive electrode and the subsequent 10 cycles were carried out under dark conditions. The figure demonstrates that a highly stable performance is maintained during the initial 10 irradiated cycles, however, turning off the laser induces a substantial increase in the charge potential alongside a concomitant decrease in the discharge potential. Comparing the tenth cycle recorded under laser irradiation with that obtained in the dark, the charge potential increased by 300 mV, whereas the discharge potential decreased by 90 mV, representing an overall voltage gap reduction of 390 mV [Figure 5D]. This improvement translates to an energy saving of 3,900 mW, which corresponds to 5.778 W g^{-1}, when related to the catalyst mass. Furthermore, when galvanostatic cycling is performed at a current of ±0.1 mA and under NIR radiation, a round-trip efficiency of 82.4%, whereas a lower value of 62.9 % was reached, in dark conditions. Furthermore, the charge/discharge potential gap decreased from 714 mV under dark conditions to 270 mV under laser irradiation, yielding a net improvement of 444 mV [Figure 5E].

The pronounced performance enhancement observed during charging is likely ascribed to the excess of hot holes generated within the AuNRs via the plasmonic effect, which are subsequently transported to the Co_3O_4 surface to drive the oxidation of O^- to O_2. Conversely, the more modest performance gain detected during discharging may also be linked to these generated holes, which are now transferred through the external circuit toward the Zn electrode, thereby lowering the overpotential required for the oxidation of Zn^0 to Zn^{2+} [Figure 5G].

Finally, Figure 5F compares the charge–discharge cycles performed at ±20 mA, showing that stable behavior is achieved under laser irradiation, with a charge/discharge potential gap of 1.33 V at the tenth cycle**.** In contrast, under dark conditions, the battery fails to maintain stable potential during discharge, dropping abruptly to 0 V, although the charging process does maintain stable potential, it exceeds 3 V.

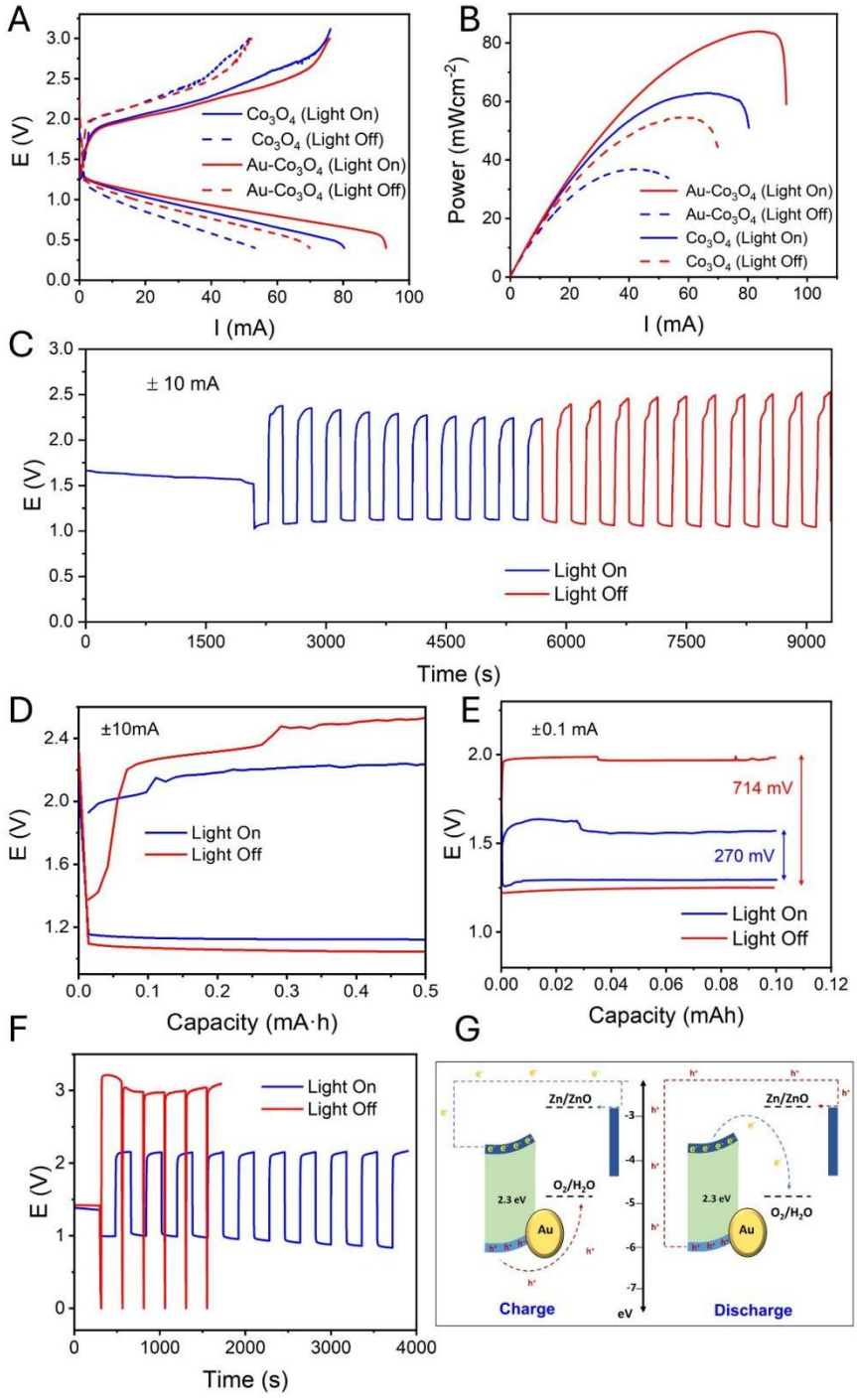


Figure 5. Polarization and Galvanostatic Charge/discharge curves obtained for ZABs including PDA@Co_3O_4@Au10 as catalyst in the air electrode, in dark and under NIR radiation. Polarization (A) and Power density-Current (B) curves; (C) 10 consecutive Galvanostatic Charge/discharge cycles obtained under NIR radiation followed by 10 cycles in the dark, all of them at ±10 mA; (D) Comparison of 10th cycle with NIR radiation versus the 10th cycle in the dark obtained at ±10 mA. (E) Comparison of the 2nd cycle with NIR radiation versus the 2nd cycle in the dark obtained at ±0.1 mA; (F) 10 consecutive Galvanostatic Charge/discharge cycles obtained under NIR radiation *vs.* 10

cycles in the dark, at ±20 mA; (G) Scheme of the operational mechanism of the plasmonic ZAB.

Furthermore, these measurements further demonstrate the enhanced catalytic performance of the PDA@Co_3O_4@Au10 material compared to PDA@Co_3O_4, highlighting the prominent contribution of the plasmonic effect of the AuNRs under NIR laser radiation, particularly toward the OER. It should be noted that current densities of 31.8 $mA \cdot cm^{-2}$ were used in these batteries (based on an electrode/electrolyte contact area of 0.63 cm^2) or 29.6 $A \cdot g^{-1}$ when expressed relative to the mass of the catalyst added to the electrode These values are higher than those previously employed in both plasmonic batteries[15,16,20,21] and other photo-assisted battery systems[8,11,12].

CONCLUSIONS

This work introduces a novel paradigm for photoactive rechargeable Zn–air batteries, leveraging the localized surface plasmon resonance induced in AuNRs-containing composites under near-infrared radiation. The synthesized composite integrates a semiconductor, such as Co_3O_4, deposited *in situ* onto a carbonaceous substrate via the calcination of a Co^{2+}-containing polymeric precursor, which enabled the homogeneous dispersion of the semiconductor within the carbon matrix. Furthermore, the incorporation of AuNRs facilitates a dark electron transfer across the heterojunction from Co_3O_4 to Au, leaving the latter with an excess of negative charge. This process establishes a potential difference at the interface, accompanied by a downward bending of both the valence and conduction bands of Co_3O_4, which subsequently blocks further electron migration toward the Au. However, the transport of holes toward the interface is energetically favored. Consequently, when a positive potential is applied to the electrode modified with the Au-containing composite, OH^- oxidation to O_2 is enhanced relative to PDA@Co_3O_4. Nevertheless, the loading of AuNRs within the composite is a critical determinant of its catalytic activity, because an excessive amount of Au blocks the active sites of Co_3O_4, thereby detrimental to the catalytic performance. Furthermore, the integration of Au into the composite does not much improve the catalytic activity toward the ORR.

Upon NIR light irradiation of the PDA@Co_3O_4@Au10 material, the oxidation process is further enhanced by the plasmonic effect occurring on the AuNRs. Under resonant excitation, hot electrons and holes are generated, and these photogenerated carriers can

be transferred into the adjacent semiconductor, thereby suppressing charge recombination. Specifically, the hot holes generated in the AuNRs transfer to the Co_3O_4, a process additionally facilitated by the band bending at the heterojunction interface, which ultimately boosts the electrocatalytic activity of the material toward the OER.

Finally, it is worth highlighting the performance enhancement observed in Zn–air batteries utilizing the positive electrode modified with the AuNRs-containing composite, particularly during the charging process, which represents a substantial reduction in recharge energy consumption. This improvement is maintained even at a high current density of 31.8 mA cm^{-2} while sustaining a potential of 1.1 V. Such operating parameters are rarely achieved in photo-assisted batteries, including lithium-based systems.

At this point, it is worth noting that the measured LSPRA determinated a photonic absorption rate enhancement of only 4.2% for the PDA@Co_3O_4@Au sample relative to PDA@Co_3O_4. Nevertheless, the improvement in energy savings achieved in the ZABs significantly exceeds this value, confirming that the charge transport dynamics facilitated by the Co_3O_4-Au junction, coupled with the plasmonic effect within the AuNRs under NIR irradiation, drives this enhanced performance.

DECLARATIONS

Acknowledgments

The authors would like to thank the technical staff of the Central Services for Research Support (SCAI) at the University of Córdoba for their technical assistance. Specifically, we express our gratitude to Juan Isidro Corredor Coca for the XPS measurements, and Francisco Gracia Alfonso, Rocío Vargas Díaz, and Carlos Medel Osuna for HR-TEM.

Authors' contributions

Conceived the idea: Giner-Casares JJ;

Designed the research and drafted the manuscript: Fernández Romero AJ, Cano M, García-Caballero V;

Synthesized and characterized the materials: García-Caballero V;

Carried out the electrocatalytic experiments: García-Caballero V, Cano M;

Performed the ZAB tests: Salazar-Ordoñez D, Fernández Romero AJ;

Performed UV-visible analysis and the photo-adsorption modelling: Calero M, Muñoz-Batista MJ;

All authors have discussed the results and given approval to the manuscript.

Availability of data and materials

The data supporting this article are available at ZENODO repository with[DOI: 10.5281/zenodo.23806285.

Supplementary information (SI): Additional data regarding physicochemical characterization (HR-XPS spectra, TEM and EDS spectra), electrochemical analysis (ECSA and OER Tafel plot).

AI and AI-assisted tools statement

During the preparation and revision of this manuscript, an AI-assisted language tool was utilized solely to improve spelling, grammar, clarity, and overall technical readability of the text (specifically within the Abstract and Introduction sections). The tool was not employed for data collection, analysis, interpretation, or the generation of scientific conclusions. Following the automated adjustments, the authors thoroughly reviewed, verified, and edited the content to ensure its accuracy, and take full responsibility for the integrity and final content of the published article.

Financial support and sponsorship

The authors would like to acknowledge financial support from MICIU/AEI/10.13039/501100011033 and FEDER/UE (PID2022-139191OB-C32 project).

Conflicts of interest

All authors declared that there are no conflicts of interest.

Ethical approval and consent to participate

Not applicable.

Consent for publication

Not applicable.

Copyright

© The Author(s) 2026.

REFERENCES

[1] F. Santos and A. J. Fernández Romero, 'Hydration as a solution to zinc batteries', *Nat. Sustain.*, vol. 5, no. 3, pp. 179-80, Dec. 2021,[DOI: 10.1038/s41893-021-00834-z]

[2] T. Li, M. Huang, X. Bai, and Y.-X. Wang, 'Metal–air batteries: A review on current status and future applications', *Progress in Natural Science: Materials International*, vol. 33, no. 2, pp. 151-71, Apr. 2023,[DOI: 10.1016/j.pnsc.2023.05.007]

[3] K. A. Jannath and H. A. Saputra, 'Transition metal-based electrocatalysts for alkaline oxygen evolution reaction: Developments, challenges, and perspectives', *Next Materials*, vol. 9, p. 101164, Oct. 2025,[DOI: 10.1016/j.nxmate.2025.101164]

[4] X.-C. Long, J.-F. Hou, H.-P. Lu, K. Yan, Q. Zhou, and L.-B. Kong, 'Molybdenum trioxide induced reconfiguration of nickel for Efficient Oxygen Evolution Reaction', *Int. J. Hydrogen Energy*, vol. 127, pp. 137-46, May 2025,[DOI: 10.1016/j.ijhydene.2025.04.181]

[5] H. H. Do, 'Recent Progress and Perspectives of Co_3O_4-Based Electrocatalysts for Oxygen Evolution Reaction', *Transactions on Electrical and Electronic Materials*, vol. 26, no. 5, pp. 667-78, Oct. 2025,[DOI: 10.1007/s42341-025-00666-0]

[6] Y. Huang, M. Zhang, P. Liu, F. Cheng, and L. Wang, 'Co_3O_4 supported on N, P-doped carbon as a bifunctional electrocatalyst for oxygen reduction and evolution reactions', *Chinese Journal of Catalysis*, vol. 37, no. 8, pp. 1249-56, Aug. 2016,[DOI: 10.1016/S1872-2067(16)62462-2]

[7] S. Liu, L. Li, H. S. Ahn, and A. Manthiram, 'Delineating the roles of Co_3O_4 and N-doped carbon nanoweb (CNW) in bifunctional Co_3O_4 /CNW catalysts for oxygen reduction and oxygen evolution reactions', *J. Mater. Chem. A Mater.*, vol. 3, no. 21, pp. 11615-23, 2015,[DOI: 10.1039/C5TA00661A]

[8] D. Du, S. Zhao, Z. Zhu, F. Li, and J. Chen, 'Photo-excited Oxygen Reduction and Oxygen Evolution Reactions Enable a High-Performance Zn–Air Battery', *Angew. Chem. Int. Ed.*, vol. 59, no. 41, pp. 18140-4, Oct. 2020,[DOI: 10.1002/anie.202005929]

[9] X. Liu *et al.*, 'Utilizing solar energy to improve the oxygen evolution reaction kinetics in zinc–air battery', *Nat. Commun.*, vol. 10, no. 1, p. 4767, Oct. 2019,[DOI: 10.1038/s41467-019-12627-2]

[10]P. Chen, T.-T. Li, Y.-B. Yang, G.-R. Li, and X.-P. Gao, 'Coupling aqueous zinc batteries and perovskite solar cells for simultaneous energy harvest, conversion and storage', *Nat. Commun.*, vol. 13, no. 1, p. 64, Jan. 2022,[DOI: 10.1038/s41467-021-27791-7]

[11]D. Zhu *et al.*, 'Photoinduced Oxygen Reduction Reaction Boosts the Output Voltage of a Zinc–Air Battery', *Angew. Chem. Int. Ed.*, vol. 58, no. 36, pp. 12460-4, Sep. 2019,[DOI: 10.1002/anie.201905954]

[12]H. Feng *et al.*, 'Photo Energy-Enhanced Oxygen Reduction and Evolution Kinetics in Zn-Air Batteries', *ACS Appl. Mater. Interfaces*, vol. 15, no. 5, pp. 6788-96, Feb. 2023,[DOI: 10.1021/acsami.2c19598]

[13]S. Linic, P. Christopher, and D. B. Ingram, 'Plasmonic-metal nanostructures for efficient conversion of solar to chemical energy', *Nat. Mater.*, vol. 10, no. 12, pp. 911-21, Dec. 2011,[DOI: 10.1038/nmat3151]

[14]M. Valenti, M. P. Jonsson, G. Biskos, A. Schmidt-Ott, and W. A. Smith, 'Plasmonic nanoparticle-semiconductor composites for efficient solar water splitting', *J. Mater. Chem. A Mater.*, vol. 4, no. 46, pp. 17891-912, 2016,[DOI: 10.1039/C6TA06405A]

[15]P. Moorthy, S. Kaliyaperumal, T. Albrecht, and K. K. Sarigamala, 'Harnessing plasmonic charge dynamics for next-generation battery chemistries', *Chemical Communications*, vol. 61, no. 73, pp. 13753-79, 2025,[DOI: 10.1039/D5CC02467F]

[16]K. Zhang *et al.*, 'Boosting Cycling Stability and Rate Capability of Li–CO_2 Batteries via Synergistic Photoelectric Effect and Plasmonic Interaction', *Angew. Chem. Int. Ed.*, vol. 61, no. 17, Apr. 2022,[DOI: 10.1002/anie.202201718]

[17]C. Zhan, X.-J. Chen, Y.-F. Huang, D.-Y. Wu, and Z.-Q. Tian, 'Plasmon-Mediated Chemical Reactions on Nanostructures Unveiled by Surface-Enhanced Raman Spectroscopy', *Acc. Chem. Res.*, vol. 52, no. 10, pp. 2784-92, Oct. 2019,[DOI: 10.1021/acs.accounts.9b00280]

[18]K. Chae, M. Kim, F. Marques Mota, and D. H. Kim, 'Disentangling plasmonic and

catalytic effects in a practical plasmon-enhanced Lithium–Oxygen battery', *J. Power Sources*, vol. 547, p. 232002, Nov. 2022,[DOI: 10.1016/j.jpowsour.2022.232002]

[19]H. Yu et al., 'Dynamic Modulation of Li_2O_2 Growth in Li-O_2 Batteries through Regulating Oxygen Reduction Kinetics with Photo-Assisted Cathodes', *Angew. Chem. Int. Ed.*, vol. 63, no. 16, Apr. 2024,[DOI: 10.1002/anie.202401272]

[20]L.-J. Zheng, F. Li, L.-N. Song, M.-L. Li, X.-X. Wang, and J.-J. Xu, 'Localized surface plasmon resonance enhanced electrochemical kinetics and product selectivity in aprotic Li–O_2 batteries', *Energy Storage Mater.*, vol. 42, pp. 618-27, Nov. 2021,[DOI: 10.1016/j.ensm.2021.08.004]

[21]Z. Ma et al., 'Efficient and Stable Photoassisted Lithium-Ion Battery Enabled by Photocathode with Synergistically Boosted Carriers Dynamics', *Nanomicro Lett.*, vol. 17, no. 1, p. 74, Dec. 2025,[DOI: 10.1007/s40820-024-01570-7]

[22]Y. Liu et al., 'Photo-assistant electrocatalytic activity improvement towards oxygen evolution', *Advanced Powder Technology*, vol. 32, no. 11, pp. 4042-8, Nov. 2021,[DOI: 10.1016/j.apt.2021.09.005]

[23]W. Mabhulusa, K. E. Sekhosana, and X. Fuku, 'The impact and performance of carbon-supported platinum group metal electrocatalysts for fuel cells', *Int. J. Electrochem. Sci.*, vol. 19, no. 4, p. 100524, Apr. 2024,[DOI: 10.1016/j.ijoes.2024.100524]

[24]K. N. Nguyen et al., 'Mott–Schottky Au/Co_3O_4 Decorated on a Carbon Cloth Substrate as an Efficiently Bifunctional Electrocatalyst for Hydrogen and Oxygen Evolution Reactions', *Energy Material Advances*, vol. 6, Jan. 2025,[DOI: 10.34133/energymatadv.0162]

[25]L. Scarabelli, A. Sánchez-Iglesias, J. Pérez-Juste, and L. M. Liz-Marzán, 'A "Tips and Tricks" Practical Guide to the Synthesis of Gold Nanorods', *J. Phys. Chem. Lett.*, vol. 6, no. 21, pp. 4270-9, Nov. 2015,[DOI: 10.1021/acs.jpclett.5b02123]

[26]N. G. Khlebtsov, B. N. Khlebtsov, E. V. Kryuchkova, S. V. Zarkov, and A. M. Burov, 'Universal Determination of Gold Concentration in Colloids with UV–vis Spectroscopy', *The Journal of Physical Chemistry C*, vol. 126, no. 45, pp. 19268-76, Nov. 2022,[DOI: 10.1021/acs.jpcc.2c05843]

[27]F. Yang et al., ‘Dopamine derived nitrogen-doped carbon sheets as anode materials for high-performance sodium ion batteries’, *Carbon N. Y.*, vol. 91, pp. 88-95, Sep. 2015,[DOI: 10.1016/j.carbon.2015.04.049]

[28]A. Parra-Marfil, M. A. Quintana, M. A. Martín-Lara, R. R. Solís, M. Calero, and M. J. Muñoz-Batista, ‘A simulator for LED photoreactors: Integrating light-matter interaction modelling and intrinsic kinetic studies for chemical engineering education’, *Education for Chemical Engineers*, vol. 55, p. 100510, Apr. 2026,[DOI: 10.1016/j.ece.2026.100510]

[29]S. Rubio et al., ‘Engineering thermo-photocatalysts via boron doping and platinum species of Bi2O3: From new materials to a novel thermo-photoreactor designed for precise control of operating conditions’, *Chemical Engineering Journal*, vol. 547, p. 180814, Nov. 2026,[DOI: 10.1016/j.cej.2026.180814]

[30]M. J. Muñoz-Batista, M. M. Ballari, A. Kubacka, O. M. Alfano, and M. Fernández-García, ‘Braiding kinetics and spectroscopy in photo-catalysis: the spectro-kinetic approach’, *Chem. Soc. Rev.*, vol. 48, no. 2, pp. 637-82, 2019,[DOI: 10.1039/C8CS00108A]

[31]D. Alba-Molina et al., ‘Bipyramidal gold nanoparticles-assisted plasmonic photothermal therapy for ocular applications’, *J. Mater. Chem. B*, vol. 13, no. 9, pp. 3000-10, 2025,[DOI: 10.1039/D4TB02688H]

[32]A. Franco et al., ‘A 2D copper-imidazolate framework without thermal treatment as an efficient ORR electrocatalyst for Zn–air batteries’, *J. Mater. Chem. A Mater.*, vol. 10, no. 46, pp. 24590-7, 2022,[DOI: 10.1039/D2TA05988F]

[33]J. Li, Y. Qin, J. Shen, and Y. Chen, ‘Evolution of carbon nanostructures during coal graphitization: Insights from X-ray diffraction and high-resolution transmission electron microscopy’, *Energy*, vol. 290, p. 130316, Mar. 2024,[DOI: 10.1016/j.energy.2024.130316]

[34]Z. Wang, M. Gao, J. Yu, W. Liu, Y. Liu, and Y. Zhai, ‘F-doped Co_3O_4/carbon composite catalyst for alkaline oxygen evolution’, *Journal of Electroanalytical Chemistry*, vol. 989, p. 119155, Jul. 2025,[DOI: 10.1016/j.jelechem.2025.119155]

[35]X. Han, F. Tang, and Z. Jin, ‘Free-standing polydopamine films generated in the

presence of different metallic ions: the comparison of reaction process and film properties', *RSC Adv.*, vol. 8, no. 33, pp. 18347-54, 2018,[DOI: 10.1039/C8RA02930J]

[36]M. A. Deyab, O. A. A. El-Shamy, M. M. Alghamdi, and A. A. El-Zahhar, 'Impact of Co_3O_4 nanoparticles on epoxy's mechanical and corrosion-resistance properties for carbon steel in seawater', *Sci. Rep.*, vol. 14, no. 1, p. 3535, Feb. 2024,[DOI: 10.1038/s41598-024-53967-4]

[37]C. Bi et al., 'Facile synthesis of hydrophilic magnetic graphene nanocomposites via dopamine self-polymerization and Michael addition for selective enrichment of N-linked glycopeptides', *Sci. Rep.*, vol. 10, no. 1, p. 71, Jan. 2020,[DOI: 10.1038/s41598-019-56944-4]

[38]A. M. Kalsin, M. Fialkowski, M. Paszewski, S. K. Smoukov, K. J. M. Bishop, and B. A. Grzybowski, 'Electrostatic Self-Assembly of Binary Nanoparticle Crystals with a Diamond-Like Lattice', *Science (1979).*, vol. 312, no. 5772, pp. 420-4, Apr. 2006,[DOI: 10.1126/science.1125124]

[39]R. Zou et al., 'Carbonized polydopamine nanoparticle reinforced graphene films with superior thermal conductivity', *Carbon N. Y.*, vol. 149, pp. 173-80, Aug. 2019,[DOI: 10.1016/j.carbon.2019.04.038]

[40]J. Amaro-Gahete et al., 'Surface Diels–Alder adducts on multilayer graphene for the generation of edge-enriched single-atom FeN_4 sites for ORR and OER electrocatalysis', *Sustain. Energy Fuels*, vol. 6, no. 6, pp. 1603- 2022,[DOI: 10.1039/D2SE00004K]

[41]J. Amaro-Gahete et al., 'FeN_4 active sites generated on dipyridylpyridazine functionalized reduced graphene oxide for high-performance air electrode in a Zn-air battery', *Journal of Electroanalytical Chemistry*, vol. 948, p. 117800, Nov. 2023,[DOI: 10.1016/j.jelechem.2023.117800]

[42]V. García-Caballero et al., 'Catalase-Based Air-Cathode for Biocompatible Zinc–Air Battery', *ChemCatChem*, vol. 17, no. 3, Feb. 2025,[DOI: 10.1002/cctc.202401343]

[43]P. Murugesh, M. Ganesan, P. S. Udaiyar, H. S. Krishnan, A. Jayaram, and N. Mani, 'Mesoporous Co_3O_4 /SnO_2 Nanostructure-Based Heterojunctions for NO_2 Sensors', *ACS Appl. Nano Mater.*, vol. 6, no. 19, pp. 17433-44, Oct. 2023,[DOI: 10.1021/acsanm.3c02327]

[44]D. Alba-Molina et al., 'Tailoring the ORR and HER electrocatalytic performances of gold nanoparticles through metal–ligand interfaces', *J. Mater. Chem. A Mater.*, vol. 7, no. 35, pp. 20425-34, 2019,[DOI: 10.1039/C9TA05492H]

[45]A. J. Young *et al.*, 'One-step synthesis and XPS investigations of chiral NHC–Au(0)/Au(i) nanoparticles', *Nanoscale*, vol. 11, no. 17, pp. 8327-33, 2019,[DOI: 10.1039/C9NR00905A]

[46]S. Noothongkaew, J. K. Han, Y. B. Lee, O. Thumthan, and K.-S. An, 'Au NPs decorated TiO2 nanotubes array candidate for UV photodetectors', *Progress in Natural Science: Materials International*, vol. 27, no. 6, pp. 641-6, Dec. 2017,[DOI: 10.1016/j.pnsc.2017.10.001]

[47]S. Wang et al., 'Precisely tuning the longitudinal localized surface plasmon resonance of gold nanorods *via* additive-regulated overgrowth', *RSC Adv.*, vol. 10, no. 21, pp. 12619-25, 2020,[DOI: 10.1039/D0RA00579G]

[48]P. Jimenéz-Calvo et al., 'A compact photoreactor for automated H2 photoproduction: Revisiting the (Pd, Pt, Au)/TiO_2 (P25) Schottky junctions', *Chemical Engineering Journal*, vol. 459, p. 141514, Mar. 2023,[DOI: 10.1016/j.cej.2023.141514]

[49]M. Tamiru Mengistu et al., *g*-C_3N_4–Co_3O_4 Z-Scheme Junction with Green-Synthesized ZnO Photocatalyst for Efficient Degradation of Methylene Blue in Aqueous Solution', *Bioinorg. Chem. Appl.*, vol. 2023, pp. 1-14, Jun. 2023,[DOI: 10.1155/2023/2948342]

[50]A. Dittmer, T. L. da Costa Gouveia, K. Sivalingam, S. DeBeer, F. Neese, and D. Maganas, 'Revisiting the band gap problem in bulk Co_3O_4 and its isostructural Zn and Al derivatives through the lens of theoretical spectroscopy', *Physical Chemistry Chemical Physics*, vol. 27, no. 33, pp. 17225-44, 2025,[DOI: 10.1039/D5CP01735A]

[51]V. Chakrapani, J. C. Angus, A. B. Anderson, S. D. Wolter, B. R. Stoner, and G. U. Sumanasekera, 'Charge Transfer Equilibria Between Diamond and an Aqueous Oxygen Electrochemical Redox Couple', *Science (1979).*, vol. 318, no. 5855, pp. 1424-30, Nov. 2007,[DOI: 10.1126/science.1148841]

[52]Y. Wang, C. Yan, H. Wang, and Y. Zhang, 'The Au nanoparticle-induced localized surface plasmon resonance effect and synergistic catalytic sites in Au/Co_3O_4 /Si pyramid

arrays for photoelectrochemical hydrogen evolution', *J. Mater. Chem. C Mater.*, vol. 13, no. 8, pp. 3944-54, 2025,[DOI: 10.1039/D4TC04087B]